3-D Single Breath-hold Shear Strain Estimation for Improved Breast Lesion Detection and Classification in Automated Volumetric Ultrasound Scanners

Gijs A.G.M. Hendriks, Chuan Chen, Hendrik H.G. Hansen, and Chris L. de Korte, *Senior Member, IEEE,*

***Abstract*—Automated breast volume scanner (ABVS) is an ultrasound imaging modality used in breast cancer screening. It has high sensitivity but limited specificity as it is hard to discriminate between benign and malignant lesions by echogenic properties. Specificity might be improved by shear strain imaging as malignant lesions, firmly-bonded to its host tissue, show different shear patterns compared to benign lesions, often loosely-bonded. Therefore, 3-D quasi-static elastography was implemented in an ABVS-like system. Plane-wave instead of conventional focussed transmissions were used to reduce scan-times within a single breath-hold. 3-D strain tensor was obtained and shear strains were reconstructed in phantoms containing firmly- and loosely-bonded lesions. Experiments were also simulated in finite-element-models (FEM). Experimental results, confirmed by FEM-results, indicated that loosely-bonded lesions showed increased maximal shear strains ($\sim 2.5\%$) and different shear patterns compared to firmly-bonded lesions ($\sim\ 0.9\%$). To conclude, we successfully implemented 3-D elastography in an ABVS-like system to assess lesion bonding by shear strain imaging.**

***Index Terms*—Automated Breast Volume Scanner, ultrasound, elastography, shear strain, breast, cancer, plane wave, quasi-static elastography**

I. Introduction

BREAST CANCER is the most commonly diagnosed type of cancer and leading cause of cancer death in women worldwide [1]. To reduce mortality and improve survival prospective, early and accurate diagnosis of breast cancer is necessary. In breast cancer detection, mammography is currently the gold standard and is based on differences in x-ray absorption between fatty and cancerous tissue. Unfortunately, mammography has a reduced sensitivity in women with dense breast tissue, i.e. the ratio non-fatty (glandular) to fatty tissue is increased.

As alternative for mammography, ultrasound imaging is widely used and is especially suitable for women with dense breasts. The limitation of ultrasound is the use of hand-held transducers resulting in an operator depending imaging method. To overcome this limitation, the automated breast volume scanner (ABVS) (Siemens healthcare, Issaquah, WA, USA) was introduced. This scanner consists of a 1-D array ultrasound transducer of 123 mm that translates over the breast while collecting ultrasound data by conventional focussed line-by-line acquisitions (scan time per volume approximately 60 s). Next, a 3-D volume of the breast can be reconstructed, and detection and classification of breast lesions can be performed based on echogenic properties of tissue structures in breast.

In the past years, several clinical studies were published that investigated the clinical performance of the ABVS and they reported high sensitivity and specificity in differentiating benign and malignant lesions [2], [3]. In these studies, patients were mostly only included if they already had a clinical reason to undergo a breast examination or biopsy. However, Wojcinski et al. [4] investigated specifically the clinical performance of the ABVS in breast cancer screening. They reported that the ABVS is a reliable imaging method with high sensitivity and fair inter-observer agreement. Conversely, they also reported a high number of false-positive results which may lead to high recall-rates, expensive second-look ultrasound examinations, and unnecessary biopsies. Therefore, improving the specificity of the ABVS would be of interest to improve breast cancer detection and screening.

Mapping of mechanical properties of different breast tissues might be a solution to improve discrimination between malignant and benign lesions, and so to increase specificity. Krouskop et al. [5] reported that Young's moduli of ductal carcinomas (300-500 kPa) were higher than for benign breast tissue (e.g. fibrous, glandular, and fatty tissue were reported to have Young's moduli of 200, 60, and 20 kPa at 20% pre-compression, respectively). Quasi-static elastography, as proposed by Ophir et al. [6], is one of the ultrasound-based methods to visualize these differences in stiffness by obtaining strain images. Briefly, pre- and post-deformation ultrasound data sets of the target tissue are recorded and cross-correlated to calculate displacements and strain values. In the past decades, quasi-static elastography has been further improved and evaluated including the development of coarse-to-fine cross-correlation based displacement estimation strategies [7], [8], the introduction of a least-square-strain estimator [9], and evaluation of the clinical performances in breast cancer detection. Sadigh et al. [10] concluded in a systematic review of clinical studies that quasi-static breast elastography has a good diagnostic performance in discriminating between benign and malignant lesions. Another development has been the expansion of quasi-static elastography to the third dimension

This work was supported by the Netherlands Organization for Scientific Research domain Applied and Engineering Sciences (NWO-TTW; Project 13290) which is partly funded by the Ministry of Economic Affairs.

G.A.G.M. Hendriks, C. Chen, H.H.G. Hansen and C.L. De Korte are with the Medical UltraSound Imaging Center, Department of Radiology and Nuclear Medicine, Radboud university medical center, Nijmegen, the Netherlands (e-mail: gijs.hendriks@radboudumc.nl; chuan.chen@radboudumc.nl; rik.hansen@radboudumc.nl; chris.dekorte@radboudumc.nl).

C.L De Korte is also with the Physics of Fluids Group, MIRA, University of Twente, Enschede, Netherlands.

This article has been accepted for publication in a future issue of this journal, but has not been fully edited. Content may change prior to final publication. Citation information: DOI 10.1109/TUFFC.2018.2849687, IEEE Transactions on Ultrasonics, Ferroelectrics, and Frequency Control

(3-D) since the introduction of 2-D array transducers [11], and 1-D array transducers that were swept in elevational direction [12], [13], [14]. In a recent study [15], we successfully implemented 3-D quasi-static elastography in a volumetric breast scanner and especially focussed on axial strain as a measure for lesion stiffness. However, besides stiffness, lesion bonding might also be an excellent choice to discriminate between benign and malignant lesions, and more specifically between fibro-adenoma and carcinoma. In the fifties, Fry [16] reported that fibro-adenoma are loosely-bonded to their surrounding tissue whereas carcinomas are firmly-bonded. Discriminating by lesion bonding would be of added value, since stiffness of fibro-adenoma and some types of carcinomas are quite similar at lower pre-compressions [5].

In 2000, it was demonstrated that it is feasible to visualise lesion mobility by ultrasound shear-strain imaging [17]. Thitaikumar et al. [18] showed in finite element simulations, phantoms and in-vivo studies that axial-shear strain distribution around a lesion is highly affected by the lesion bonding. The potential of shear-strain imaging in lesion classification was confirmed by Xu et al. [19]. Their study (123 patients) resulted in a sensitivity and specificity of 0.86 and 0.80 respectively in classifying breast lesions by normalised axial shear-strain distributions. In these and other studies [20], [21], only the axial-shear strain component is used to evaluate lesion bonding since this component is of superior quality compared to the lateral-shear component. In the axial-shear-strain-approach, the operator has to rotate the probe until the maximum shearing occurs in the 2-D imaging plane. In 3-D, we want to avoid this user dependency and therefore a parameter is required which is not depending on imaging plane or the direction of shearing. Hence, we propose the maximal shear strain parameter, since it does not only take into account the axial-lateral shear component but also all other shear strain components. Multiple approaches have been developed to calculate the (3-D) strain tensor (e.g. Lagrangian speckle model estimators [22], [23]; multilevel hybrid strain algorithms [24] and normalized cross-correlation). In this study, we implemented iterative multilevel normalized cross-correlation [25] and least-squares-strain estimation [9] to calculate the entire 3-D strain tensor.

First steps in the implementation of elastography in the ABVS were shown in recent studies [15], [26]. Tyagi et al. [26] proposed a method to obtain shear moduli in breast tissue by conventional ABVS scanning. Although initial results are promising, this method has some practical limitations. To prevent and correct for motion and breathing artefacts, 20 volumes had to be obtained with a total scan time of ± 15 minutes. Plane-wave imaging can reduce the scan times such that two entire volumes can be obtained within one breath-hold. Furthermore, post-processing times and data storage space can be reduced when only two volumes have to be processed to calculate elastic properties. Finally, this study only used the axial displacement component to determine mechanical properties, whereas lateral and elevational displacement, and (shear-) strain components might provide additional information about breast lesions and tissue.

Therefore, in this study, quasi-static elastography was implemented in a 3-D ABVS-like system to reconstruct the entire 3-D strain tensor and to enable evaluation of all (shear-) strain components. To prevent breathing artefacts in future $in-vivo$ examinations, scan times were decreased below one breath-hold (< 10 s) by ultrasound plane-wave instead of conventional line-by-line acquisitions. Summarized, the aim of this study was to verify whether it was possible to implement 3-D volumetric shear-strain imaging combined with plane-wave acquisitions in an ABVS-like system to improve lesion discrimination by bonding.

II. Materials and Methods

A. Plane-wave imaging

Plane-wave imaging is an ultrasound technique [27], [28] in which multiple subsequent elements (e.g. 128) are excited with fixed difference in delay between adjacent elements to generate an unfocused so-called plane wave. Subsequent, the reflected and scattered radio-frequency (RF) signals are collected for each transducer element (RF-element data). Finally beam-formed RF-data can be reconstructed from RF-element data by applying a beam-forming algorithm. In this study, we utilize delay-and-sum (DAS), a technique based on the expected time-of-flight in the RF-element data, to reconstruct every point defined in the ultrasound grid [29]. The used ultrasound grid had a resolution of 21 μm (axial, ± 6 points per wavelength) and 82 μm (lateral, 2.4 points per pitch). Furthermore, apodization (70 $\%$ hamming window) and an F-number of 0.875 were implemented in receive. As the RF-element-data were recorded frame-by-frame in ABVS-like scanning, the RF-data were also beam-formed frame-by-frame.

B. Displacement estimation

Axial, lateral, and elevational displacements (u_z, u_x and u_y respectively) were calculated by cross-correlation of pre- and post-deformation beam-formed RF-data volumes. An iterative 3-D cross-correlation algorithm was used to calculate the displacements [30], [15], [25]. In the first step, 3-D cross-correlation was performed on axially down-sampled envelope data (factor eight) to find a coarse estimate of the displacements. In subsequent steps, the search kernel size was reduced and 3-D cross-correlation was performed on RF-data with the displacement of the previous iteration as offset to calculate more accurate displacements at sample level. As finer kernel settings were used in every subsequent iteration, the spacing in the displacement grid also decreased for each iteration (table I). In the final iteration, displacements were calculated for every single frame in the elevational direction (500 μm), every 15 sample points axially (315 μm), and every 4 lines laterally (328 μm), resulting in axial and lateral kernel overlaps of 60% and 80%, respectively. The window and kernel sizes, and displacement grid settings for all iterations were based on [31] and can be found in table I. After the final iteration, the cross-correlation peak of each displacement point was interpolated (3-D, spline) to calculate displacements on subsample level.

TABLE I
OVERVIEW OF KERNEL AND SEARCH WINDOW SIZES, AND RESOLUTION OF THE DISPLACEMENT GRID FOR EACH ITERATION. ENVELOPE DATA (ENV) WERE USED IN THE FIRST ITERATION AND RF-DATA IN ALL SUBSEQUENT ITERATIONS.

Iteration	Kernel (ax x lat x ele) μm^3	Window (ax x lat x ele) μm^3	Resolution (ax x lat x ele) μm
$1-env$†	$4200\ x\ 820\ x\ 1500$	$8400\ x\ 1722\ x\ 4500$	$2520\ x\ 2624\ x\ 500$
$2-RF$	$2100\ x\ 820\ x\ 1500$	$4200\ x\ 1722\ x\ 4500$	$1260\ x\ 1312\ x\ 500$
$3-RF$	$1050\ x\ 410\ x\ 1500$	$2100\ x\ \ 902\ x\ 4500$	$630\ x\ \ 656\ x\ 500$
$4-RF$	$525\ x\ 410\ x\ 1500$	$1050\ x\ \ 902\ x\ 4500$	$315\ x\ \ 328\ x\ 500$

†Axially and laterally down-sampled (factor six and two respectively).

C. Strain estimation

11-by-1 point least-square-strain estimation [9] was used to calculate the following strain components (s):

$$s_{i,j} = \frac{\partial u_i}{\partial x_j}, \tag{1}$$

with u_i displacements in i direction derived to x_j in j direction, $i \in (x, y, z)$, and $j \in (x, y, z)$. Axial, lateral and elevational directions are represented by z, x and y respectively.

The 3-D strain tensor was reconstructed by these components according to the next equation:

$$\varepsilon_{i,j} = \begin{bmatrix} \varepsilon_{xx} & \varepsilon_{xy} & \varepsilon_{xz} \\ \varepsilon_{yx} & \varepsilon_{yy} & \varepsilon_{yz} \\ \varepsilon_{zx} & \varepsilon_{zy} & \varepsilon_{zz} \end{bmatrix} = \begin{bmatrix} s_{xx} & \frac{s_{xy}+s_{yx}}{2} & \frac{s_{xz}+s_{zx}}{2} \\ \frac{s_{yx}+s_{xy}}{2} & s_{yy} & \frac{s_{yz}+s_{zy}}{2} \\ \frac{s_{zx}+s_{xz}}{2} & \frac{s_{zy}+s_{yz}}{2} & s_{zz} \end{bmatrix}. \tag{2}$$

To calculate the 3-D maximal shear strain ($\varepsilon_{3Dshear}$), first the three eigenvalues of the strain tensor were calculated which represent the principal strains ($\varepsilon_{prin1,\ 2\ and\ 3}$). The difference between the maximal and minimal principal strain values (ε_{prin1} and ε_{prin3}, respectively) represents the maximal shear strain [32]:

$$\varepsilon_{3Dshear} = \frac{\varepsilon_{prin1} - \varepsilon_{prin3}}{2}, \tag{3}$$

with $\varepsilon_{prin1} \geq \varepsilon_{prin2}$ and $\varepsilon_{prin2} \geq \varepsilon_{prin3}$

As the elevational resolution might be insufficient for displacement and strain estimations, the 2-D maximal shear strain ($\varepsilon_{2Dshear}$) was also calculated analogous to $\varepsilon_{3Dshear}$ but neglecting the elevational strain components:

$$\varepsilon_{2Dshear} = \frac{\varepsilon_{prin1} - \varepsilon_{prin2}}{2}, \tag{4}$$

with $\varepsilon_{prin1} \geq \varepsilon_{prin2}$

D. Shear-strain phantom

Two block phantoms (40 mm x 40 mm x 40 mm) containing each an ellipse-shaped lesion were made from polyvinyl alcohol (PVA) (Mw $85,000$-$124,000$; Sigma-Aldrich GmbH, Steinheim, Germany) with 1% silica scatter particles (silica gel 60, 0.015-0.040 mm; Merck KGaA, Darmstadt, Germany) as described by Surry et al. [33]. To ensure homogeneous freezing of the phantom and homogeneous mechanical properties, PVA was dissolved in 60% demineralized water and 40% ethylene glycol (technically suitable as anti-freezing liquid; Sigma-Aldrich GmbH, Steinheim, Germany). Phantom 1 contained a lesion that was firmly bonded to its surrounding whereas phantom 2 contained a loosely bonded lesion. To produce different kind of bonding situations, first lesions (ellipsoid; length, width, and height of 8.5, 8.5, and 10 mm respectively) were made by freeze-thawing a 10% PVA solution once. Next, only the loosely-bonded lesion was coated with a thin layer of latex. Liquid PVA solution (7.5%) was poured at $40°$C in two block-shaped moulds in which the lesions were hung by a wire in the mould centre. The coated lesion did not bond to its surrounding whereas the other non-coated lesion could be considered as bonded due to cross-linking of the lesion PVA with the surrounding PVA. Finally, the block phantom underwent two freeze-thaw cycles. Afterwards, the lesion-to-surrounding ratio of axial strain ($\varepsilon_{zz_{lesion}} : \varepsilon_{zz_{surrounding}}$) was experimentally determined as approximately $4:1$ in both phantoms. This ratio was also used in the finite element simulations.

E. Experiment

The two shear-strain phantoms were positioned under a custom-build translational stage that enabled vertical and horizontal translation of a mounted L12-5 50 mm transducer (ATL, Bothell, WA, USA) that was connected to a Verasonics V1 ultrasound research system (Verasonics, Kirkland, WA, USA) to enable plane-wave imaging. An ultrasound transparent membrane (S2000, Siemens healthcare, Issaquah, WA, USA) was positioned between the phantom and ultrasound transducer. To collect pre-deformation data, element data were recorded every 0.5 mm (elevational direction) by plane-wave acquisitions. As this transducer was multiplexed by subsets of subsequent 128 elements, three sub-acquisitions were used to cover the entire field-of-view. Therefore, a plane wave was transmitted by a sub-set of the first, centre and last 128 elements, and received by the first, centre and final 85 elements respectively. All sub-acquisitions were subsequently acquired with 8 kHz, which we consider to be a high enough pulse repetition rate to assume all sub-acquisitions were acquired at equal elevational position. The transducer translated with a constant speed 20 mm·s^{-1} while collecting data. According to [15] and [34], collected RF-data, and displacement and strain

estimates are minimally affected by this speed. Thereafter, the acquisitions were repeated but the transducer and membrane were lowered (0.5 mm axially) to ensure deformation of the entire phantom and not only under the transducer surface. Next, element data were collected post-deformation. The entire protocol was performed for both phantoms. After the data collection, the obtained ultrasound data were beam-formed, and displacements and strain were calculated as described earlier.

F. Finite element model

To compare experimental with theoretically expected results and to evaluate different degrees of bonding, the experiments were also simulated by a finite element model similar as in [18] but extended to the third dimension in this study. Therefore, the experimental phantoms were mimicked in the finite element package ANSYS Mechanical 17.2 (ANSYS, Canonsburg, PA, USA). A block phantom (40 mm x 40 mm x 40 mm; Young's modulus 20 kPa) was simulated with an ellipse-shaped lesion (length, width, and height of 8.5, 8.5, and 10 mm respectively; 80 kPa) and an angle of 15° between the longest lesion axis and axial ultrasound axis to match the experimental configuration. The Young's modulus ratio (lesion to surrounding) was similar as the same strain ratio in the experiments (see C. Shear-strain phantom). For the simulations, the bottom plane was fixed; axial (z) displacement of 0.5 mm was applied homogeneously to the top lateral-elevational (x-y) plane and all side planes were free to displace. The coefficient of friction between the surfaces of the inclusion and surrounding was varied between 0.001 (fully loosely) and 10 (firmly bonded) to simulate different levels of lesion bonding. This coefficient is the ratio of the frictional resistance and normal force acting between two surfaces. Next, the simulated displacements were exported and interpolated from the mesh grid positions to the same displacement grid used for the experimental data. Finally, the strain components were calculated as described before.

G. Post-processing

Elastographic signal-to-noise ratio (SNR) and contrast-to-noise ratio (CNR) of the shear strain results ($\varepsilon_{2Dshear}$ and $\varepsilon_{3Dshear}$) were calculated [35]:

$$SNR = \frac{S_{signal}}{\sigma_{signal}}, \tag{5}$$

$$CNR = \frac{2(S_{signal} - S_{background})^2}{\sigma^2_{signal} + \sigma^2_{background}}. \tag{6}$$

The shear strain values in a 4.5 mm thick shell around the lesion were considered as signal (S_{signal}). The background signal ($S_{background}$) was represented by shear strain values measured in two spheres right and left above the lesion, see Fig. 1.

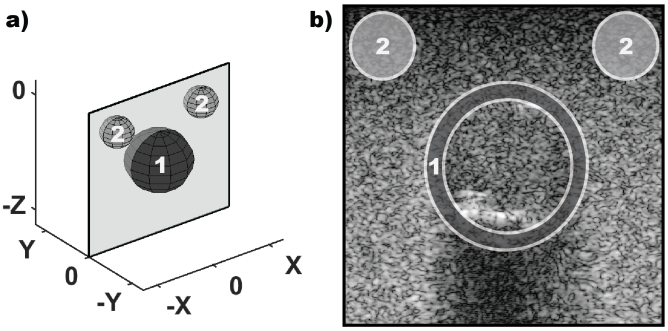

Fig. 1. a) 3-D visualisation of region-of-interest (ROI) of S_{signal} (1) and $S_{background}$ (2) used to calculate SNR and CNR values. The ROI of (1) includes only a 450 μm thick area around the annotated lesion; b) example of experimentally acquired log-compressed B-mode image of the XZ-plane through the centre of the loosely-bonded lesion with the ROI of (1) and (2) indicated. The position of the background ROI was similar as in [31], [35], but extended to the third dimension.

III. Results

A. Displacements

In Fig. 2 and 3, the lateral (u_x), elevational (u_y) and axial (u_z) displacement fields of both phantoms as obtained by simulations and experiments are visualized. Since a z-deformation (0.5 mm) was applied, it was expected that u_z showed a gradient from 0 to 0.5 mm, which was confirmed by both the simulated and experimental results in both phantoms (Fig. 2c, f, and 3c, f). Furthermore, the u_x and u_y were expected to have a range between -0.25 and $+0.25$ mm as incompressibility was assumed as can be seen in the simulated results in Fig. 2. In the experimental results (Fig. 3), this range could also be observed for u_x in both phantoms (Fig. 3a and 3d). The simulations showed also this gradient in u_y (Fig. 2b and 2e). However, it was not observed in the experimental results (Fig. 3b and 3e). This might be caused by the transducer pushing forward the phantom after lowering the transducer axially which was not modelled for the simulated displacements. Note that the expected u_y, between -0.25 and 0.25 mm, was smaller than the elevational inter-frame distance (0.5 mm).

An observation was that the displacement gradient rotated 90° inside the loosely bonded lesion compared to the surrounding tissue for u_x and u_z (Fig. 2a,c; 3a,c) which was also reported in [36]. This rotation in gradient was especially visible in the gradient (s) of the displacements in perpendicular direction (e.g. u_x in z-direction, see Fig. 4 and 5). Since the ellipsoid lesion was only slightly rotated in the xz-plane, rotation was limited in the y-direction (Fig. 4c and 5c). Consequently, the gradient was not rotated inside the lesion compared to the surrounding tissue (Fig. 2b). The small increase of s_{yz} around the loosely bonded lesion (Fig. 5c) may be caused by the transducer movement, especially since this increase was not observed in the simulations (Fig. 4c) in which this movement was not modeled. Rotation was not observed in the firmly bonded lesion as rotation and shear were restricted by the high degree of connectivity (Fig. 4d-f and 5d-f).

This article has been accepted for publication in a future issue of this journal, but has not been fully edited. Content may change prior to final publication. Citation information: DOI 10.1109/TUFFC.2018.2849687, IEEE Transactions on Ultrasonics, Ferroelectrics, and Frequency Control

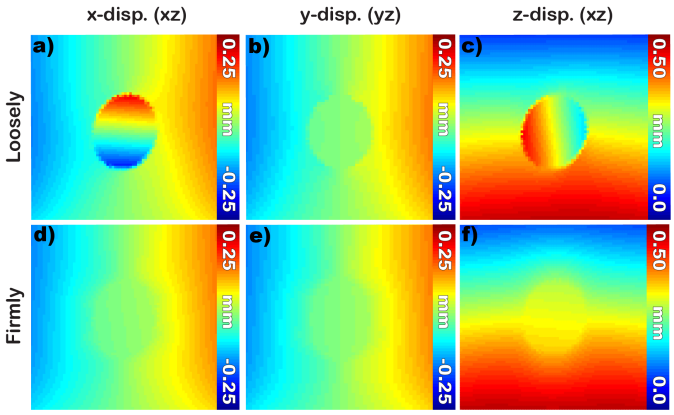

Fig. 2. Lateral (u_x), elevational (u_y) and axial (u_z) displacements fields by finite element model for loosely and firmly bonded phantom. Displacements u_x and u_z were visualized in the xz-plane, and u_y in the yz-plane. All planes cut through the middle of the lesion. The dimensions of all figures were 25 mm x 25 mm, and the middle of the transducer was assumed as $x = 0$ and $z = 0$; the middle frame as $y = 0$.

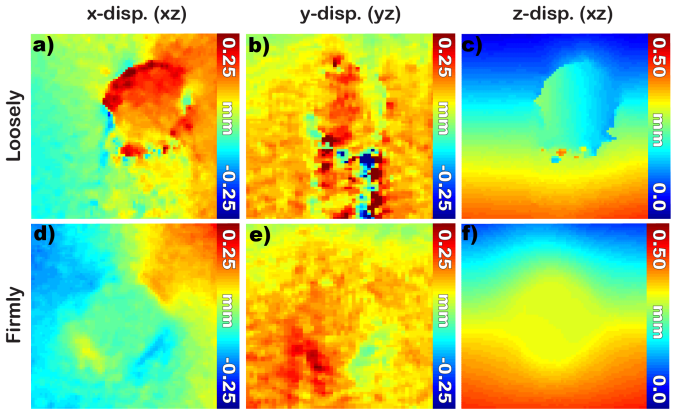

Fig. 3. Lateral (u_x), elevational (u_y) and axial (u_z) fields by the experiments for loosely and firmly bonded phantom. Displacements u_x and u_z were visualized in the xz-plane, and uy in the yz-plane. All planes cut through the middle of the lesion. The dimensions of all figures were 25 mm x 25 mm.

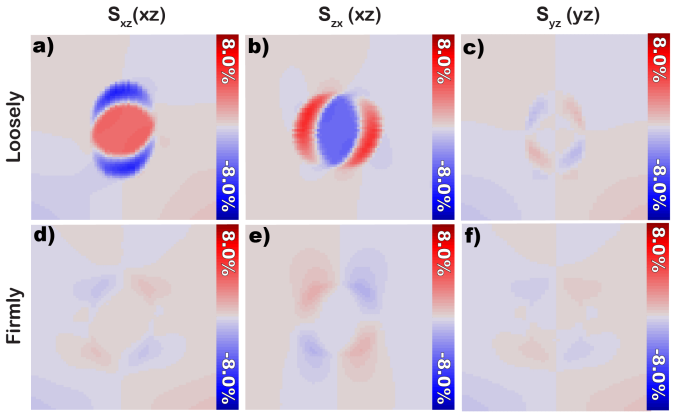

Fig. 4. Images of the gradient (s) of the finite element model lateral (x), axial (z) and elevational (y) displacements in axial (s_{xz}), lateral (s_{zx}) and axial direction (s_{yz}), respectively. All planes (xz and xy) cut through the middle of the loosely or firmly bonded lesion. The dimensions of all figures were (25 mm x 25 mm).

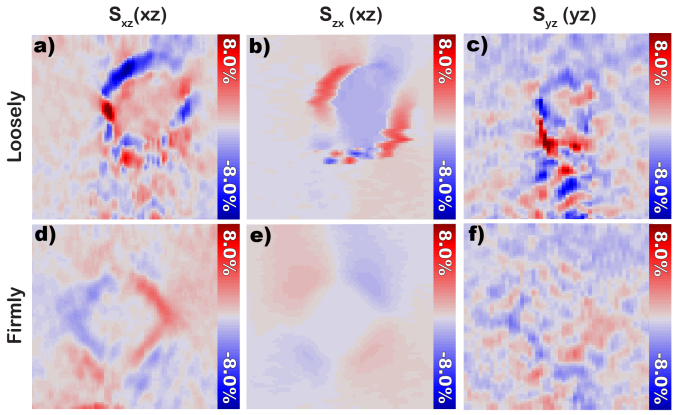

Fig. 5. Images of the gradient (s) of the experimental lateral (x), axial (z) and elevational (y) displacements in axial (s_{xz}), lateral (s_{zx}) and axial direction (s_{yz}), respectively. All planes (xz and xy) cut through the middle of the loosely or firmly bonded lesion. The dimensions of all figures were (25 mm x 25 mm).

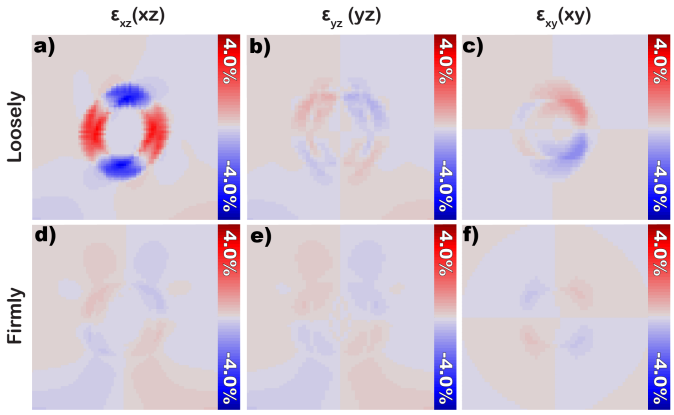

Fig. 6. Shear components (ε_{xz}, ε_{yz} and ε_{xy}) of the simulated loosely and firmly bonded lesions. The components are visualized in the planes (25 mm x 25 mm) they act on and cut through the centre of the lesion.

B. Shear-strain components

The next step was to inspect the three shear components of the strain tensor (2). First observation in the simulated results was that the absolute shear strain in the xz-plane (ε_{xz}) was increased ($\pm 3.5\%$) around the loosely bonded lesion (Fig. 6a) compared to the other components ($\pm 2.0\%$) (Fig. 6b-c). Rotation of the lesion was mainly expected in the xz-plane due to the geometry of the lesion. Compared to the loosely bonded lesion, the firmly bonded lesion showed much smaller absolute shear strain values for all components (Fig. 6). Similar patterns and intensities were also visible in the experimental data as can be seen in Fig. 7. However, the absolute intensities of the shear in yz- and xy-plane were also increased compared to the simulated results, indicating rotation might have occurred in y-direction. The components that were partly estimated by y-displacements resulted in images with increased noise levels (Fig. 7b-c and 7e-f), which can be explained by the reduced accuracy of elevational displacement estimation (Fig. 3b-e).

This article has been accepted for publication in a future issue of this journal, but has not been fully edited. Content may change prior to final publication. Citation information: DOI 10.1109/TUFFC.2018.2849687, IEEE Transactions on Ultrasonics, Ferroelectrics, and Frequency Control

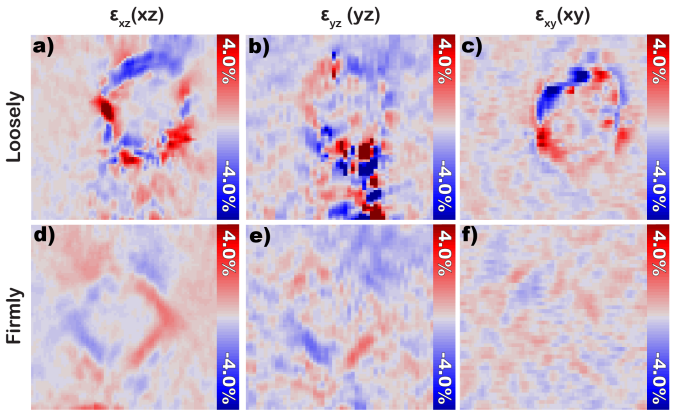

Fig. 7. Shear components (ε_{xz}, ε_{yz} and ε_{xy}) of loosely and firmly bonded lesions by the experiments. The components are visualized in the planes (25 mm x 25 mm) they act on and cut through the centre of the lesion.

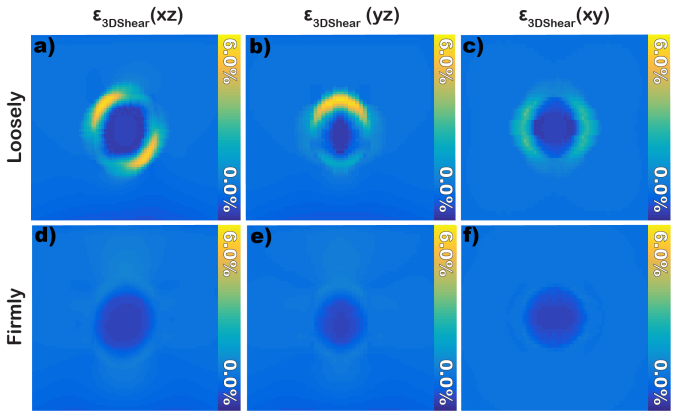

Fig. 8. Maximal shear strain ($\varepsilon_{3DShear}$) calculated using all components of the strain tensor. $\varepsilon_{3DShear}$ of the loosely and firmly bonded lesion by finite element modelling is visualized in the xz-plane that cut through the centre of the lesion, and the yz- and xy-plane that cut through the left quarter and upper quarter of the lesion respectively.

C. Maximal shear strain

In the final step, the maximal shear strain was calculated by the reconstructed shear strain tensor (2). The results of the simulations and experiments can be seen in Fig. 8 and 9, respectively. Note that the yz- and xy-planes are planes cutting through the inclusion of the upper and left quarter of the inclusion respectively instead of through the centre as in the previous figures. The highest intensity of the shear strain ($> 3.7\%$) was observed in the right upper and bottom lower part around the loosely-bonded lesion in both simulated and experimental results (Fig. 8a-c and 9a-c). The two areas with increased shear strain corresponded to areas along the long axes of the ellipsoid lesion. In the firmly bonded lesion, the shear strain was increased minimally ($< 1.4\%$) around the lesion (Fig. 8d-f, 9d-f). Furthermore, the experimental and simulated results seemed to show similar shear strain patterns and values.

In Fig. 10, the maximal shear strain of the experimental (loosely and firmly bonded lesion) and of the simulated results (lesion with different degree of bonding) were presented. The shear strain intensity decreases with an increasing degree of friction in the simulated results which was confirmed by the experimental results. In Fig. 10a, the entire halo around the lesion was used as signal area, whereas in Fig. 10b only the upper-left part was used. In the latter area, the difference between loosely and firmly was even stronger as only the area in which high shear strain occurred was evaluated. The shear strain values ($25th$, $50th$ and $75th$ quartile) and the related SNR- and CNR-values were summarized in table II (rows indicated by 3-D).

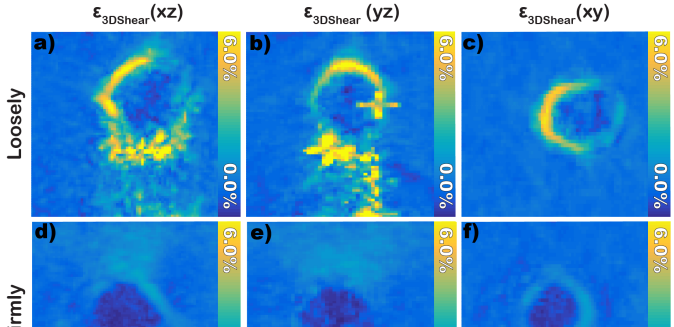

Fig. 9. Maximal shear strain ($\varepsilon_{3DShear}$) calculated using all components of the strain tensor. $\varepsilon_{3DShear}$ of the loosely and firmly bonded lesion by measurements is visualized in the xz-plane that cut through the centre of the lesion, and the yz- and xy-plane that cut through the left quarter and upper quarter of the lesion respectively.

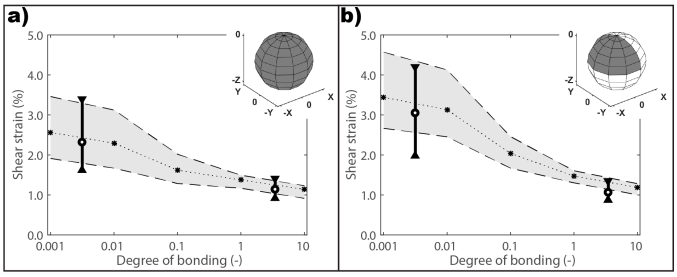

Fig. 10. Overview of the maximal shear strain ($\varepsilon_{3DShear}$) in the full halo (a) and left-upper quarter halo (b) around the lesion, indicated by the dark gray area of the sphere in the right corners. The halo thickness was half the mean radius of the lesion. The experimental shear strain was visualized as open dot ($50th$ percentile) and error bars ($25th$ and $75th$ percentile); Results of the loosely (degree of bonding towards 0) and firmly bonded lesion (degree of bonding more than 1) were plotted at the left and right side of the graph, the corresponding degree of bonding was an approximate since the exact degree of bonding could not be determined. The finite element data was plotted for each simulated degree of bonding similar to the experimental data whereas the filled dots represent the $50th$ percentile, and the lower and upper limit of the gray area (dashed lines) the $25th$ and $75th$ percentile.

D. 2-D and 3-D maximal shear strain

In Fig. 8, 9 and 10, the maximal shear strain ($\varepsilon_{3Dshear}$) was calculated using all nine components in the strain tensor (2). As displacement u_y suffer from reduced accuracy (Fig. 3b,e), an option was to calculate the maximal shear strain by only the components acting in the xz-plane ($\varepsilon_{2Dshear}$). These results can be seen in table II (rows indicated by 2-D), and Fig. 11 and 12. In both the simulated and experimental results,

TABLE II

OVERVIEW OF THE MAXIMAL SHEAR STRAIN VALUES ($25th$, $50th$ AND $75th$ QUARTILE), SNR AND CNR VALUES OF THE LOOSELY AND FIRMLY BONDED LESION OF THE FINITE ELEMENT SIMULATIONS (SIM) AND EXPERIMENTS (EXP) CALCULATED BY ALL STRAIN TENSOR COMPONENTS (3-D) AND ONLY COMPONENTS ACTING IN THE XZ-PLANE (2-D). ALL VALUES WERE PROVIDED USING THE FULL AND THE UPPER-LEFT QUARTER HALO AROUND THE LESION AS SIGNAL. IN THIS TABLE, A DEGREE OF BONDING OF 0.001 AND 10 WERE USED IN THE SIMULATIONS FOR THE LOOSELY AND FIRMLY BONDED LESION RESPECTIVELY.

	Full halo					Upper-left quarter halo				
	ε_{25th} (%)	ε_{50th} (%)	ε_{75th} (%)	SNR (dB)	CNR (dB)	ε_{25th} (%)	ε_{50th} (%)	ε_{75th} (%)	SNR (dB)	CNR (dB)
Loosely Sim 2-D	1.4	2.2	3.2	5.2	6.2	2.3	3.2	4.3	7.6	14
3-D	1.9	2.6	3.5	7.1	11	2.7	3.4	4.6	9.0	17
Exp 2-D	1.0	1.5	2.5	3.7	5.8	1.2	2.5	3.7	4.8	11
3-D	1.6	2.3	3.4	4.6	8.2	2.0	3.1	4.2	6.9	14
Firmly Sim 2-D	0.82	1.0	1.2	13	−7.4	0.90	1.1	1.2	13	−21
3-D	0.92	1.1	1.2	14	−11	1.0	1.2	1.3	14	−32
Exp 2-D	0.57	0.8	1.2	5.9	−24	0.63	0.90	1.2	7.7	−16
3-D	0.92	1.1	1.4	10	−6.5	0.87	1.1	1.4	10	−11

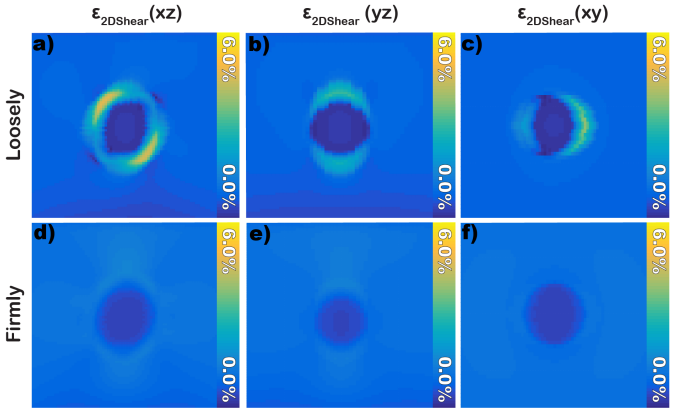

Fig. 11. Maximal shear strain ($\varepsilon_{2DShear}$) calculated using only x and z components of the strain tensor and the y components were neglected, i.e. assumed zero. $\varepsilon_{2DShear}$ of the loosely and firmly bonded lesion by finite element modelling is visualized in the xz-plane that cut through the center of the lesion, and the yz- and xy-plane that cut through the left quarter and upper quarter of the lesion respectively.

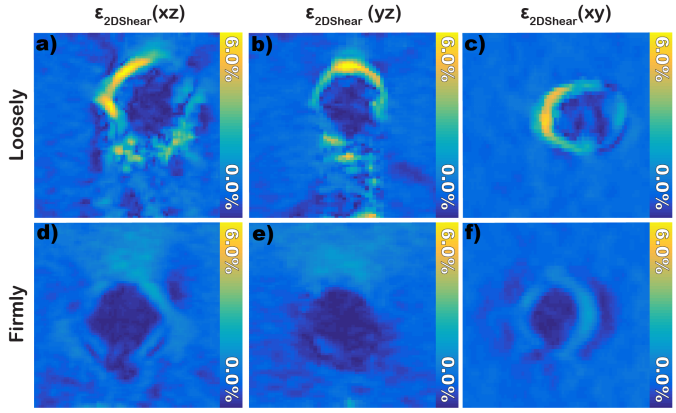

Fig. 12. Maximal shear strain ($\varepsilon_{2DShear}$) calculated using only x and z components of the strain tensor and the y components were neglected, i.e. assumed zero. $\varepsilon_{2DShear}$ of the loosely and firmly bonded lesion by measurements is visualized in the xz-plane that cut through the center of the lesion, and the yz- and xy-plane that cut through the left quarter and upper quarter of the lesion respectively.

the intensity, SNR and CNR of $\varepsilon_{2Dshear}$ were decreased compared to $\varepsilon_{3Dshear}$ except for the CNR in the simulated results of the firmly bonded lesion. This exception can be explained by a more homogeneous background signal used to calculat the CNR. This decrease was expected as shear in elevational direction was neglected resulting in lower maximal shear strain intensities which can also be seen comparing Fig. 8 ($\varepsilon_{3Dshear}$) and 11 ($\varepsilon_{2Dshear}$). The CNR in firmly bonded lesion were negative for experiments and simulations, indicating that the contrast between the maximal shear strain and background was smaller than the variance of the signal and background. This can also be seen in Fig. 9 and 11 in which the shear strain around the lesion was hardly visible.

IV. DISCUSSION

A. Maximal shear strain

The main observation was that shear strains ($\varepsilon_{2Dshear}$ and $\varepsilon_{3Dshear}$) of both lesion types showed similar patterns and intensities in simulations and experiments (Fig. 10) and that the loosely bonded lesion showed increased shear-strain values in the halo region (Fig. 10) with sufficient SNR and CNR values for detection (table II), whereas these values were decreased for the firmly bonded lesion. Consequently, shear strain in the latter lesion type was similar to the background signal resulting in low CNR values. Shear strains were especially visible at the top-left and bottom-right of the lesion (Fig. 8, 9, 11, and 12) which was caused by the geometry and rotation of the lesion and the applied deformation. The shear strain estimates seemed to be less accurate under the loosely-bonded lesion (Fig. 9a-b). This was also visible in the lateral and elevational displacement estimates (Fig. 3a-b). The latex coating around this lesion type introduced a shadowing artefact (see the shadowing below the lesion in Fig. 1b) which can explain the reduced accuracy in this area. This coating artefact would not be expected *in-vivo*.

B. Lateral displacements

The gradient s_{xz}, which is based on lateral displacement estimates, showed similar values and patterns as the simulated results, although the results were noisier compared to the s_{zx} derivative which is based on axial displacement estimates (Fig. 4 and 5). This difference between estimated lateral and axial displacements can also be noticed in Fig. 3. The main explanation is that in the axial direction phase information was available which improved the displacement estimates, whereas in the lateral and elevational direction this information was lacking. In the most recently published studies [21], [37], [20], [19], the gradient s_{zx} was used as a measure for shear strain and lesion bonding as the s_{xz} component was insufficient for reconstructing ε_{xz}.

In this study, ε_{xz} and consequently maximal shear strain was reconstructed as the lateral displacement estimates were of sufficient quality. Three possible explanations, or a combination of these, could contribute to improved accuracy of lateral displacements in this study. First, lateral displacements may be estimated more robustly using 3-D instead of 1-D or 2-D ultrasound data and search kernels for cross-correlation. Another explanation might be that plane-wave acquisitions were implemented and RF-data were reconstructed to a beamforming grid with multiple A-lines per pitch. This principle can be considered partly similar to interpolation of conventional line-by-line acquired ultrasound RF-data in the lateral direction to improve lateral displacement estimates [38], [39]. This improvement was confirmed by Hendriks et al. [40] in which the effect of multiple A-lines per pitch on the accuracy of lateral displacement estimates in plane-wave imaging was investigated. A third explanation might be the implementation of 3-D spline interpolation of cross-correlation peaks to obtain sub-sample displacements. In previous studies, 1-D cosine and 1-D parabolic interpolation were often implemented to estimate axial and lateral sub-sample displacements independently from each other. In this study, 3-D spline interpolation was used in which axial, lateral and elevational sub-sample displacement estimations were coupled. According to Azar et al. [41] and Saris et al. [42], 2-D or 3-D peak interpolation improves lateral sub-sample displacement estimates and so might explain the improved lateral displacement estimates in this study.

Although, the lateral displacement estimates seem to be of sufficient quality, the axial displacements were still superior. A strategy to improve the lateral displacement estimates might be spatial compounding in which large insonification angles are used to reconstruct lateral displacements [43], [31]. Since RF-phase information is incorporated in the displacement estimations, it is expected that the lateral displacements can be estimated more accurately. Another strategy might be to improve the lateral resolution in the RF-data itself by coherent compounding [44]. In this strategy, multiple insonification angles are used to reconstruct the RF-data and so to decrease the lateral point-spread-function. Note that in the latter strategy, the ultrasound RF-data are compounded prior to displacement estimation in contrast to spatial compounding in which displacements are compounded after displacement estimation of RF-data of individual insonification angles. Next the improved lateral displacements estimates, a benefit of both spatial and coherent compounding might reduce the estimation noise induced by shadowing artefacts (Fig. 1b, 3a-b) due to multiple insonification angles.

C. Elevational displacements

As can be seen in the experimental elevational displacements (u_y) (Fig. 3b, e), these displacement estimates were less accurate compared to the lateral and especially axial estimates (Fig. 3). The inter-frame distance was 0.5 mm while u_y was expected to be less than 0.5 mm. Consequently, u_y could only be estimated by interpolation of the cross-correlation peak. Solutions to obtain more accurate elevational displacement estimates might be to decrease the inter-frame distance or interpolation of ultrasound data to a denser grid. Although these solutions seem straight forward, a concern might be the extra amount of collected and stored ultrasound data and increased processing time. Furthermore, Lopata et al. [7] showed that interpolation of the cross-correlation peak, which was applied in this study, and A-line up-sampling resulted in similar performance in sub-pitch displacement estimation. A combination of A-line up-sampling with a lower interpolation factor and cross-correlation peak interpolation might be good trade-off between estimation accuracy and computational load [45] to improve the accuracy of elevational displacement estimates.

Although elevational displacement estimation might be less accurate, it seemed to contribute to increased signal, SNR and CNR of the maximal shear strain comparing $\varepsilon_{3Dshear}$ and $\varepsilon_{2Dshear}$, especially in the loosely bonded lesion (table II). Note that the maximal shear strain in this study (experiments and simulations) were expected to occur predominately in the xz-plane as the lesion was slightly tilted in this plane. Therefore, the added value of the shear components in which the elevational displacements were involved might even be more increased when the lesion was tilted in the other planes (xy and yz). Furthermore, the transducer might also induce shear strain in the elevational direction due to translation contributing to $\varepsilon_{3Dshear}$. This translation might explain the increased signal difference between $\varepsilon_{2Dshear}$ and $\varepsilon_{3Dshear}$ in the experimental compared to simulation results, as this effect was not considered in the finite element model.

D. Clinical implementation

The results showed that it was possible to obtain multiple measures for lesion bonding all based on shearing of the lesion: s_{zx}, ε_{xz} and maximal shear strain ($\varepsilon_{2Dshear}$ and $\varepsilon_{3Dshear}$). s_{zx}, the gradient of axial displacements in the lateral direction, was used in many studies in the past as measure for shear strain. The shear in the XZ plane (ε_{xz}) could not be reconstructed in these studies as the accuracy of the lateral displacements was insufficient. However, in this study, the lateral displacements were sufficient to reconstruct ε_{xz} and the maximal shear strain. Future clinical studies have to evaluate which parameter will be most robust to be used to discriminate between loosely (benign) and firmly (malignant)

lesions. One can speculate that combining more gradient and shear components, so more information, to reconstruct ε_{xz} or the maximal shear strain may result in a more robust measure to evaluate lesion bonding. However, this will always be a trade- off between adding information and adding noise influenced by the accuracy of the estimate for the different components. This effect of adding noise could be observed in the comparison between $\varepsilon_{2Dshear}$ (Fig. 12) and $\varepsilon_{3Dshear}$ (Fig. 9): in the latter the border of lesion was less visible probably due to the influence of the reduced accuracy of the elevational components.

This study mainly focussed on the feasibility of 3-D shear strain estimation for breast lesion classification and the effect of different degrees of lesion bonding. However, lesion geometry and position might also affect shear strain estimates. In this study, a slightly tilted elliptic lesion with different degrees of bonding was investigated. However, other geometries and tilting angles were also possible (e.g. elliptic lesion with an angle 45° to the transducer surface might induce higher shear strains compared to similar lesion parallel to the surface). Invasive ductal carcinoma (IDC) originates in ducts and starts growing in the duct before becoming invasive resulting in an elliptic geometry with the long axis along the duct. As ducts connect the nipple with deeper located lobules, the long axis will almost always be rotated to the transducer and skin surface which is optimal for inducing shear strains by slightly deforming the tissue in axial direction. Benign lesions (cysts and fibro-adenoma) can have different geometries and rotations. According to Xu et al [46], s_{zx} and ε_{xz} are not affected by lesion size or shape but mainly by bonding. It is also of interest to investigate the effect of geometry on $\varepsilon_{2Dshear}$ and $\varepsilon_{3Dshear}$ in future studies.

The advantage of plane-wave imaging was the increased frame rate. In conventional ultrasound, each frame is reconstructed line-by-line by focussed ultrasound transmission. Consequently, the acquisition time of one volume in the ABVS is ± 60 seconds introducing breathing artefacts and these will especially affect future elastographic measurements. In plane-wave imaging, one frame can be acquired by one plane-wave transmission. For a 192 channel ultrasound system, the speed-up can be up to 192, reducing the acquisition times to even below one second, far below one breath-hold to avoid breathing artefacts. Due to image quality deterioration in plane-wave imaging mode, coherent compounding might be required still resulting in a full scan time of less than 5 seconds.

V. Conclusions

Based on the results of this study, we can conclude that it is feasible to implement shear strain imaging in an ABVS-like system to detect lesion bonding. It was shown by phantom experiments and finite element modelling that maximal shear strain was strongly correlated to lesion bonding, i.e. firmly and loosely bonded lesions could be discriminated by measuring the maximal shear strain around the lesion. Furthermore, plane-wave imaging was implemented to reduce the acquisition times to enable volumetric scanning within a breath-hold which is required in future $in-vivo$ applications.

Acknowledgment

The authors would like to thank Jan Menssen, Anne Saris and Stein Fekkes for their technical support and constructive discussions.

References

[1] L. A. Torre, F. Bray, R. L. Siegel, J. Ferlay, J. Lortet-Tieulent, and A. Jemal, "Global cancer statistics, 2012," *CA Cancer J Clin*, vol. 65, no. 2, pp. 87–108, 2015.

[2] Y. W. Kim, S. K. Kim, H. J. Youn, E. J. Choi, and S. H. Jung, "The clinical utility of automated breast volume scanner: a pilot study of 139 cases," *J Breast Cancer*, vol. 16, no. 3, pp. 329–34, 2013.

[3] Z. Meng, C. Chen, Y. Zhu, S. Zhang, C. Wei, B. Hu, L. Yu, B. Hu, and E. Shen, "Diagnostic performance of the automated breast volume scanner: a systematic review of inter-rater reliability/agreement and meta-analysis of diagnostic accuracy for differentiating benign and malignant breast lesions," *Eur Radiol*, vol. 25, no. 12, pp. 3638–47, 2015.

[4] S. Wojcinski, S. Gyapong, A. Farrokh, P. Soergel, P. Hillemanns, and F. Degenhardt, "Diagnostic performance and inter-observer concordance in lesion detection with the automated breast volume scanner (abvs)," *BMC Med Imaging*, vol. 13, p. 36, 2013.

[5] T. A. Krouskop, T. M. Wheeler, F. Kallel, B. S. Garra, and T. Hall, "Elastic moduli of breast and prostate tissues under compression," *Ultrasonic Imaging*, vol. 20, no. 4, pp. 260–274, 1998.

[6] J. Ophir, I. Cespedes, H. Ponnekanti, Y. Yazdi, and X. Li, "Elastography: a quantitative method for imaging the elasticity of biological tissues," *Ultrason Imaging*, vol. 13, no. 2, pp. 111–34, 1991. [Online]. Available: http://www.ncbi.nlm.nih.gov/pubmed/1858217

[7] R. G. Lopata, M. M. Nillesen, H. H. Hansen, I. H. Gerrits, J. M. Thijssen, and C. L. de Korte, "Performance evaluation of methods for two-dimensional displacement and strain estimation using ultrasound radio frequency data," *Ultrasound Med Biol*, vol. 35, no. 5, pp. 796–812, 2009. [Online]. Available: http://www.ncbi.nlm.nih.gov/pubmed/19282094

[8] H. Shi and T. Varghese, "Two-dimensional multi-level strain estimation for discontinuous tissue," *Phys.Med.Biol.*, vol. 52, no. 2, pp. 389–401, 2007. [Online]. Available: PM:17202622

[9] F. Kallel and J. Ophir, "A least-squares strain estimator for elastography," *Ultrason Imaging*, vol. 19, no. 3, pp. 195–208, 1997.

[10] G. Sadigh, R. C. Carlos, C. H. Neal, and B. A. Dwamena, "Accuracy of quantitative ultrasound elastography for differentiation of malignant and benign breast abnormalities: a meta-analysis," *Breast Cancer Res Treat*, vol. 134, no. 3, pp. 923–31, 2012.

[11] T. G. Fisher, T. J. Hall, S. Panda, M. S. Richards, P. E. Barbone, J. Jiang, J. Resnick, and S. Barnes, "Volumetric elasticity imaging with a 2-d cmut array," *Ultrasound in Medicine & Biology*, vol. 36, no. 6, pp. 978–990, 2010. [Online]. Available: http://www.sciencedirect.com/science/article/pii/S0301562910001419

[12] S. Bharat, T. G. Fisher, T. Varghese, T. J. Hall, J. Jiang, E. L. Madsen, J. A. Zagzebski, and F. T. Lee Jr, "Three-dimensional electrode displacement elastography using the siemens c7f2 foursight four-dimensional ultrasound transducer," *Ultrasound in Medicine & Biology*, vol. 34, no. 8, pp. 1307–1316, 2008. [Online]. Available: http://www.sciencedirect.com/science/article/pii/S0301562908000124

[13] J. E. Lindop, G. M. Treece, A. H. Gee, and R. W. Prager, "3d elastography using freehand ultrasound," *Ultrasound Med Biol*, vol. 32, no. 4, pp. 529–45, 2006.

[14] H. Rivaz, I. Fleming, L. Assumpcao, G. Fichtinger, U. Hamper, M. Choti, G. Hager, and E. Boctor, "Ablation monitoring with elastography: 2d in-vivo and 3d ex-vivo studies," *Med Image Comput Comput Assist Interv*, vol. 11, no. Pt 2, pp. 458–66, 2008.

[15] G. A. Hendriks, B. Hollander, J. Menssen, A. Milkowski, H. H. Hansen, and C. L. de Korte, "Automated 3d ultrasound elastography of the breast: a phantom validation study," *Phys Med Biol*, vol. 61, no. 7, pp. 2665–79, 2016.

[16] K. E. Fry, "Benign lesions of the breast," *CA: A Cancer Journal for Clinicians*, vol. 4, no. 5, pp. 160–161, 1954. [Online]. Available: http://dx.doi.org/10.3322/canjclin.4.5.160

[17] E. E. Konofagou, T. Harrigan, and J. Ophir, "Shear strain estimation and lesion mobility assessment in elastography," *Ultrasonics*, vol. 38, no. 1-8, pp. 400–4, 2000.

[18] A. Thitaikumar, T. A. Krouskop, B. S. Garra, and J. Ophir, "Visualization of bonding at an inclusion boundary using axial-shear strain elastography: a feasibility study," *Phys Med Biol*, vol. 52, no. 9, pp. 2615–33, 2007.

[19] H. Xu, T. Varghese, J. Jiang, and J. A. Zagzebski, "In vivo classification of breast masses using features derived from axial-strain and axial-shear images," *Ultrason Imaging*, vol. 34, no. 4, pp. 222–36, 2012.

[20] H. Xu, M. Rao, T. Varghese, A. Sommer, S. Baker, T. J. Hall, G. A. Sisney, and E. S. Burnside, "Axial-shear strain imaging for differentiating benign and malignant breast masses," *Ultrasound Med Biol*, vol. 36, no. 11, pp. 1813–24, 2010. [Online]. Available: http://www.ncbi.nlm.nih.gov/pubmed/20800948

[21] A. K. Thittai, B. Galaz, and J. Ophir, "On the advantages of imaging the axial-shear strain component of the total shear strain in breast tumors," *Ultrasound Med Biol*, vol. 38, no. 11, pp. 2031–7, 2012.

[22] R. L. Maurice and M. Bertrand, "Lagrangian speckle model and tissue-motion estimation-theory [ultrasonography]," *IEEE Transactions on Medical Imaging*, vol. 18, no. 7, pp. 593–603, July 1999.

[23] R. L. Maurice, J. Ohayon, G. Finet, and G. Cloutier, "Adapting the lagrangian speckle model estimator for endovascular elastography: Theory and validation with simulated radio-frequency data," *The Journal of the Acoustical Society of America*, vol. 116, no. 2, pp. 1276–1286, 2004. [Online]. Available: https://doi.org/10.1121/1.1771615

[24] H. Chen and T. Varghese, "Multilevel hybrid 2d strain imaging algorithm for ultrasound sector phased arrays," *Medical Physics*, vol. 36, no. 6Part1, pp. 2098–2106, 2009. [Online]. Available: http://dx.doi.org/10.1118/1.3121426

[25] R. G. Lopata, M. M. Nillesen, J. M. Thijssen, L. Kapusta, and C. L. de Korte, "Three-dimensional cardiac strain imaging in healthy children using rf-data," *Ultrasound Med Biol*, vol. 37, no. 9, pp. 1399–408, 2011. [Online]. Available: http://www.ncbi.nlm.nih.gov/pubmed/21767901

[26] M. Tyagi, Y. Wang, T. J. Hall, P. E. Barbone, and A. A. Oberai, "Improving three-dimensional mechanical imaging of breast lesions with principal component analysis," *Med Phys*, vol. 44, no. 8, pp. 4194–4203, 2017.

[27] B. Delannoy, R. Torguet, C. Bruneel, and E. Bridoux, *Ultrafast Electronical Image Reconstruction Device*. Dordrecht: Springer Netherlands, 1979, ch. 59, pp. 447–450.

[28] B. Delannoy, R. Torguet, C. Bruneel, E. Bridoux, J. M. Rouvaen, and H. Lasota, "Acoustical image reconstruction in parallel processing analog electronic systems," *Journal of Applied Physics*, vol. 50, no. 5, pp. 3153–3159, 1979. [Online]. Available: http://aip.scitation.org/doi/abs/10.1063/1.326397

[29] H. H. Hansen, A. E. Saris, N. R. Vaka, M. M. Nillesen, and C. L. de Korte, "Ultrafast vascular strain compounding using plane wave transmission," *J Biomech*, vol. 47, no. 4, pp. 815–23, 2014.

[30] S. Fekkes, A. E. Swillens, H. H. Hansen, A. E. Saris, M. M. Nillesen, F. Iannaccone, P. Segers, and C. L. de Korte, "2-d versus 3-d cross-correlation-based radial and circumferential strain estimation using multiplane 2-d ultrafast ultrasound in a 3-d atherosclerotic carotid artery model," *IEEE Trans Ultrason Ferroelectr Freq Control*, vol. 63, no. 10, pp. 1543–1553, 2016. [Online]. Available: http://www.ncbi.nlm.nih.gov/pubmed/27576246

[31] H. H. Hansen, R. G. Lopata, T. Idzenga, and C. L. de Korte, "Full 2d displacement vector and strain tensor estimation for superficial tissue using beam-steered ultrasound imaging," *Phys Med Biol*, vol. 55, no. 11, pp. 3201–18, 2010.

[32] C. Oomens, M. Brekelmans, and F. Baaijens, *Stress in three-dimensional continous media*. New York, NY, United States of America: Cambridge University Press, 2009, ch. 8, pp. 132–152.

[33] K. J. M. Surry, H. J. B. Austin, A. Fenster, and T. M. Peters, "Poly(vinyl alcohol) cryogel phantoms for use in ultrasound and mr imaging," *Physics in Medicine and Biology*, vol. 49, no. 24, pp. 5529–5546, 2004.

[34] B. Hollnder, G. A. Hendriks, R. M. Mann, H. H. Hansen, and C. L. de Korte, "Plane-wave compounding in automated breast volume scanning: A phantom-based study," *Ultrasound in Medicine and Biology*, vol. 42, no. 10, pp. 2493 – 2503, 2016. [Online]. Available: http://www.sciencedirect.com/science/article/pii/S0301562916300989

[35] U. Techavipoo and T. Varghese, "Improvements in elastographic contrast-to-noise ratio using spatial-angular compounding," *Ultrasound Med Biol*, vol. 31, no. 4, pp. 529–36, 2005.

[36] A. Kothawala, S. Chandramoorthi, N. R. K. Reddy, and A. K. Thittai", ""spatial compounding technique to obtain rotation elastogram: A feasibility study"," *"Ultrasound in Medicine and Biology"*, vol. "43", no. "6", pp. "1290 – 1301", "2017". [Online]. Available: "http://www.sciencedirect.com/science/article/pii/S030156291730056X"

[37] A. K. Thittai, J. M. Yamal, L. M. Mobbs, C. M. Kraemer-Chant, S. Chekuri, B. S. Garra, and J. Ophir, "Axial-shear strain elastography for breast lesion classification: further results from in vivo data," *Ultrasound Med Biol*, vol. 37, no. 2, pp. 189–97, 2011.

[38] J. Luo and E. E. Konofagou, "Effects of various parameters on lateral displacement estimation in ultrasound elastography," *Ultrasound Med Biol*, vol. 35, no. 8, pp. 1352–66, 2009.

[39] J. Ophir, S. K. Alam, B. Garra, F. Kallel, E. Konofagou, T. Krouskop, and T. Varghese, "Elastography: ultrasonic estimation and imaging of the elastic properties of tissues," *Proc Inst Mech Eng H*, vol. 213, no. 3, pp. 203–33, 1999.

[40] G. A. Hendriks, C. Chen, H. H. Hansen, and C. L. de Korte, "Quasi-static elastography and ultrasound plane-wave imaging: The effect of beam-forming strategies on the accuracy of displacement estimations," *Applied Sciences*, vol. 8, no. 3, 2018. [Online]. Available: http://www.mdpi.com/2076-3417/8/3/319

[41] R. Z. Azar, O. Goksel, and S. E. Salcudean, "Sub-sample displacement estimation from digitized ultrasound rf signals using multi-dimensional polynomial fitting of the cross-correlation function," *IEEE Transactions on Ultrasonics, Ferroelectrics, and Frequency Control*, vol. 57, no. 11, pp. 2403–2420, November 2010.

[42] A. E. C. M. Saris, S. Fekkes, M. M. Nillesen, H. H. G. Hansen, and C. L. de Korte, "A psf-shape-based beamforming strategy for robust 2d motion estimation in ultrafast data," *Applied Sciences*, vol. 8, no. 3, 2018. [Online]. Available: http://www.mdpi.com/2076-3417/8/3/429

[43] M. Rao and T. Varghese, "Spatial angular compounding for elastography without the incompressibility assumption," *Ultrason.Imaging*, vol. 27, no. 4, pp. 256–270, 2005. [Online]. Available: PM:16761786

[44] G. Montaldo, M. Tanter, J. Bercoff, N. Benech, and M. Fink, "Coherent plane-wave compounding for very high frame rate ultrasonography and transient elastography," *IEEE Trans Ultrason Ferroelectr Freq Control*, vol. 56, no. 3, pp. 489–506, 2009.

[45] Z. Liu, C. Huang, and J. Luo, "A systematic investigation of lateral estimation using various interpolation approaches in conventional ultrasound imaging," *IEEE Transactions on Ultrasonics, Ferroelectrics, and Frequency Control*, vol. 64, no. 8, pp. 1149–1160, Aug 2017.

[46] H. Xu, T. Varghese, and E. L. Madsen, "Analysis of shear strain imaging for classifying breast masses: Finite element and phantom results," *Medical Physics*, vol. 38, no. 11, pp. 6119–6127, 2011. [Online]. Available: http://dx.doi.org/10.1118/1.3651461

Gijs A.G.M. Hendriks received the M.Sc degree in biomedical engineering from the Eindhoven University of Technology (TU/e), Eindhoven, The Netherlands in 2014. As part of his M.Sc program, he did an internship at the Newcastle Magnetic Resonance Centre, Newcastle University, Newcastle-upon-Tyne, U.K. in 2012. Under the supervision of P. Thelwall, he worked on the development of an MRI scanning protocol to obtain concentrations of metabolites, fat, and other molecules of interest in skeletal muscle of patients suffering from dysferlinopathy. Thereafter, he completed his graduate project in the research groups of Peter Hilbers (Computational Biology) and Klaas Nicolay (Biomedical NMR) in the Department of Biomedical Engineering, TU/e. During this project, he investigated energy metabolism in human skeletal muscle during exercise by combining in vivo 31P-MRS measurements and computational modeling. Currently, he is pursuing his Ph.D. degree on the project entitled 3-D ultrasound elastography for detection of tumours in breast at the Medical Ultrasound Imaging Centre, Radboud University Medical Center, Nijmegen, The Netherlands. This project is a close collaboration with Siemens Healthineers, Issaquah, WA. His current research interests include developing ultrafast functional ultrasound techniques in breast cancer imaging.

Chuan Chen was born in Jiujiang, China, in 1992. He received the bachelors degree from the Huazhong University of Science and Technology, Wuhan, China, in 2013, the masters degree in electrical engineering from the Eindhoven University of Technology, Eindhoven, The Netherlands. Currently, he is Ph.D student at the Medical Ultrasound Imaging Centre, Radboudumc, Nijmegen, The Netherlands. He works on the project Ultrafast 3-D elastography for tumor detection in breast, under the supervision of Prof. C. de Korte. His current research interests include ultrafast ultrasound, acoustic signal and image processing, and biotissue functional imaging.

Hendrik (Rik) H.G. Hansen received the M.Sc. degree in applied physics from the Eindhoven University of Technology, Eindhoven, The Netherlands, in 2005, and the Ph.D. degree in noninvasive vascular ultrasound strain elastography for vulnerable plaque detection in carotid arteries from Radboud University Medical Center, Nijmegen, The Netherlands, in 2012. He was a Software/System Test Engineer with Assemblon BV, Veldhoven, The Netherlands. Since 2007, he has been with the Medical UltraSound Imaging Center (MUSIC), Radboud University Medical Center. Since 2017, he has been the Leader of the Functional Ultrasound Imaging Workgroup, MUSIC. He has authored or co-authored over 30 peer-reviewed scientific articles in national and international journals and two book chapters. His current research interests include developing ultrafast functional ultrasound techniques, such as 3-D strain elastography, 3-D blood flow imaging and shear wave elastography for vascular applications, and breast cancer detection.

Chris L. de Korte received the M.Sc. degree in electrical engineering from the Eindhoven University of Technology, Eindhoven, The Netherlands, in 1993, and the Ph.D. degree in medical sciences from the Thoraxcenter, Erasmus University Rotterdam, Rotterdam, The Netherlands, in 1999, with a focus on intravascular ultrasound elastography. In 2002, he joined the Clinical Physics Laboratory, Radboud University Nijmegen Medical Center, Nijmegen, The Netherlands, as an Assistant Professor and became its head in 2004. In 2006, he was appointed an Associate Professor of medical ultrasound techniques and completed his training as a Medical Physicist in 2007. Since 2012, he has been head of the Medical UltraSound Imaging Center, Department of Radiology and Nuclear Medicine, Nijmegen. He was appointed Full Professor of medical ultrasound techniques in 2015. He has authored or co-authored over 150 peer-reviewed articles in international journals, and is the inventor or co-inventor of four patents. His current research interests include functional imaging, acoustical and mechanical tissue characterization, and photo-acoustic imaging, all using ultrasound for cardiovascular applications and diagnosis, treatment monitoring, and guiding interventions in oncological applications. Dr. de Korte was a recipient of the EUROSON Young Investigator Award 1998 from the European Federation of Societies for Ultrasound in Medicine and Biology. He is the President of the Netherlands Society for Medical Ultrasound.